Science Bulletin 64 (2019) 1024–1030

Contents lists available at ScienceDirect

Science Bulletin

journal homepage: www.elsevier.com/locate/scib

Article

Approaching the minimum lattice thermal conductivity of p-type SnTe thermoelectric materials by Sb and Mg alloying

Tiezheng Fu, Jiazhan Xin, Tiejun Zhu *, Jiajun Shen, Teng Fang, Xinbing Zhao *

State Key Laboratory of Silicon Materials, and School of Materials Science and Engineering, Zhejiang University, Hangzhou 310027, China

ARTICLE INFO

Article history:
Received 2 April 2019
Received in revised form 14 May 2019
Accepted 27 May 2019
Available online 6 June 2019

Keywords:
Tin telluride
Thermoelectric materials
Point defect scattering
Band convergence

ABSTRACT

SnTe, as the nontoxic analogue to high-performance PbTe thermoelectric material, has captured the worldwide interest recently. Many triumphant instances focus on the strategies of band convergence, resonant doping, and nano-precipitates phonon scattering. Herein, the p-type SnTe-based materials $Sn_{0.85-x}Sb_{0.15}Mg_xTe$ (x = 0–0.10) are fabricated and a combined effect of Sb and Mg is investigated. Sb alloying tunes the hole carrier concentration of SnTe and decreases the lattice thermal conductivity. Mg alloying leads to a nearly hundredfold rise of disorder parameter due to the large mass and strain fluctuations, and as a consequence the lattice thermal conductivity decreases further down to ~0.64 W m^{-1} K^{-1} at 773 K, close to the theoretical minimum of the lattice thermal conductivity (~0.50 W m^{-1} K^{-1}) of SnTe. In conjunction with the enhancement of the Seebeck coefficient caused by band convergence due to Mg alloying, the maximum zT_{max} reaches ~1.02 and the device zT_{device} of ~0.50 at 773 K for $Sn_{0.79}Sb_{0.15}Mg_{0.06}Te$, suggesting this SnTe-based composition has a promising potential in intermediate temperature thermoelectric applications.

1. Introduction

In past decades, the emphasis on worldwide development is transferring from a rapid and barbaric mode to a greener, more sustainable one. So, as a burgeoning type of energy materials, thermoelectric (TE) materials have attracted increasing attention, because they can convert waste heat to electricity directly with many advantages such as miniature, light weight, no moving parts, long life, etc. [1–8]. The conversion efficiency of TE devices is restricted by the Carnot efficiency and the dimensionless figure of merit zT, $zT = \alpha^2\sigma T/(\kappa_e + \kappa_L)$, where α, σ, κ_e, κ_L and T represent the Seebeck coefficient, the electrical conductivity, the electronic thermal conductivity, the lattice thermal conductivity, and the absolute temperature, respectively [9–14]. In order to enhance the conversion efficiency, a high Seebeck coefficient, a high electrical conductivity and a low thermal conductivity are required. However, these parameters are interrelated through carrier concentration and it is hard to adjust only one of them independently. Fortunately, owing to persevering pursuit, various decoupling strategies have been proposed and high performance TE materials have made a great progress [15–22].

Lead telluride, one of the earliest and most studied TE materials, has reached very high zTs (p-type: zT_{max} ~ 2.5 at 923 K [23,24]; n-type: zT_{max} ~ 1.8 at 773 K [25,26]) in the intermediate temperature range. A homogeneous large bulk (~200 g, Φ 42 mm × 18 mm) of p-type PbTe with average zT > 2 has also been obtained [27]. However, the call for non-toxic and eco-friendly TE materials limits the further application of PbTe-based materials. So SnTe, the lead-free analogue of PbTe, has recently received more and more attention [28,29].

Pristine SnTe contains high concentrations of intrinsic Sn vacancies and exhibits a hole overdoped (10^{20}–10^{21} cm^3) TE transport behavior [30–32]. Although SnTe has two valence bands in electronic structure similar to PbTe, the energy separation between the light valence band at the L point and the heavy valence band at the Σ point is so large (0.35 eV at 300 K versus 0.12 eV for PbTe) that the Σ band does little contribution to carrier transport process and the Seebeck coefficient, not to mention that the small band gap (0.15 eV at 300 K) of SnTe is more likely to make the bipolar effect happen [33–35]. Meanwhile, SnTe has a high lattice thermal conductivity (~3.5 W m^{-1} K^{-1} at 300 K). As a result, pristine SnTe owns inferior TE properties.

However, by enhancing the electrical properties and reducing the thermal conductivity, a significant zT enhancement has been achieved for SnTe. Banik et al. [36] and Wang et al. [37] found that a large amount of Sb alloying in SnTe could reduce the lattice

* Corresponding authors.
E-mail addresses: zhutj@zju.edu.cn (T. Zhu), zhaoxb@zju.edu.cn (X. Zhao).

https://doi.org/10.1016/j.scib.2019.06.007
2095-9273/

thermal conductivity due to the intergrowth layered Sb-rich nano-precipitates and result in a figure of merit $zT \sim 0.9$ at 800 and 923 K. Introducing interstitial Cu atoms also leads to the enhanced scattering of phonons and an ultra-low lattice thermal conductivity ($\sim$0.5 W m^{-1} K^{-1} at 850 K) [38]. Alloying some tellurides like CdTe [39,40], MnTe [35,41–43], MgTe [34], CaTe [33], etc. in SnTe could increase the Seebeck coefficient sharply by band convergence between the heavy Σ and light L valence band, and the band gap would become broader as well. Resonant level induced by indium doping in SnTe also induces the similar enhancement of the Seebeck coefficient [44]. These efforts make SnTe a promising TE material for substituting the lead telluride.

In this work, taking $Sn_{0.85}Sb_{0.15}Te$ as a matrix due to its lowest lattice thermal conductivity reported in previous literature [36], we further explore the effect of Mg addition on the TE performance of $Sn_{0.85}Sb_{0.15}Te$ to study the synergistic effect of Mg and Sb co-alloying in SnTe-based system. Light element Mg not only introduces large mass and strain fluctuations in matrix to reduce lattice thermal conductivity, but also facilitates band degeneracy and enhances Seebeck coefficient. In order to utilize SnTe-based TE materials reliably, it is also beneficial to shift the maximum zT_{max} to lower temperature and raise the device zT_{device} among the whole temperature range. Eventually, we obtained a $zT_{max} \sim 1.02$ and a $zT_{device} \sim 0.50$ for $Sn_{0.79}Sb_{0.15}Mg_{0.06}Te$ at 773 K, which are the competitive values at such low temperatures.

2. Experimental

2.1. Synthesis

Polycrystalline $Sn_{0.85-x}Sb_{0.15}Mg_xTe$ (x = 0, 0.02, 0.04, 0.06, 0.08 and 0.10) samples were synthesized by melting, ball milling and hot pressing. According to the stoichiometric ratio, the raw materials of Sn (granular, 99.999%), Sb (chunk, 99.999%), Mg (turnings, 99.8%), Te (chunk, 99.999%) were weighed and loaded into carbon-coated quartz tubes. The tubes were sealed under a residual pressure of $\sim 10^{-4}$ Pa, slowly heated to 1,173 K over 12 h, soaked for 10 h, and then cooled down to room temperature slowly. The ingots were crushed and ball milled (Mixer Mill MM200, Retsch) for 30 min. The fine powders ($\sim$0.2–0.6 μm) were hot pressed (HP-5x7-GG-2200-VM-G-25 T, Materials Research Furnace) in a graphite die of Φ12.7 mm at 800 K under 80 MPa and eventually the disk-shaped pellets with approximately 2 mm thickness were obtained. The relative densities of all the samples are no less than 93%.

2.2. Characterization

The phase structures were analyzed by X-ray diffraction (XRD, Rigaku D/MAX 2550/PC) with monochromatic Cu Kα radiation, and the microstructures and chemical compositions of the samples were investigated by electron probe microanalysis (EPMA, JEOL JXA-8100). The fresh fracture surfaces of the samples were observed by scanning electron microscope (SEM, Hitachi S-4800).

2.3. Thermoelectric measurements

The thermal conductivity was calculated by using the equation $\kappa = D\rho C_p$, in which D is the thermal diffusivity, ρ is the geometric density and C_p is the heat capacity. The value of D was measured by Netzsch LFA 457 Micro Flash Analyzer with an uncertainty of ±3% and the density was measured by the Archimedes method. The heat capacity was estimated by C_p (k_B/atom) = 3.07 + 0.00047 (T/K–300) for lead chalcogenides [45,46] and tin telluride [35,38], which was obtained by fitting the experimental data reported by Blachnik and Igel [47]. A home-made computer-aided thermoelectric measurement apparatus using a DC four-probe and differential voltage/temperature technique was applied to measure the Seebeck coefficient and electrical conductivity of the samples with both uncertainties of ±5% [48]. The Hall coefficient R_H was measured under 2 T magnetic field at 300 K by using a Mini Cryogen Free Measurement Systems, with an uncertainty of ±10%. The carrier concentration n_H and the carrier mobility μ_H were computed by $n_H = 1/eR_H$ and $\mu_H = \sigma R_H$, respectively. The transverse and longitudinal sound velocities of all bulk samples at room temperature were measured by using a Panametrics 5052 pulser/receiver with the filter at 0.03 MHz and a Tektronic TDS5054B-NV digital oscilloscope. The coefficient of linear expansion α_l was measured by using Netzsch DIL 402 PC.

3. Results and discussion

3.1. Phase structure

The powder XRD patterns of $Sn_{0.85-x}Sb_{0.15}Mg_xTe$ (x = 0, 0.02, 0.04, 0.06, 0.08 and 0.10) samples are illustrated in Fig. 1a. The main phase could be indexed as the NaCl-type crystal structure (space group *Fm-3m*) and a trace amount of second phases can be observed in all samples. Due to the solubility limit of Sb in SnTe to be 9 at%–12 at% [36,37], the second phases can be ascribed to the excess Sb but cannot be identified at present. The rough thin curve shown in Fig. 1b is derived by taking the logarithm of the diffraction pattern for the $Sn_{0.85}Sb_{0.15}Te$ sample, together with the JCPDS standard cards of several phases chosen according to the ternary phase diagram of SnTe-Sb_2Te_3 as Fig. 1e [49] (the curve of SbTe in Fig. 1b was calculated via Materials Studio®). Similar situation also occurred in previous study, in which the weak impurity peaks in the XRD patterns of $Sn_{0.85}Sb_{0.15}Te$ could not be identified and by using transmission electron microscopy (TEM) the second phases in $Sn_{0.85}Sb_{0.15}Te$ were deduced to be the nanoscale layered intergrowth Sb-rich $(SnTe)_m(Sb_2Te_3)_n$ [36,37].

Fig. 1c and d shows the back-scattering electron (BSE) image of the polished surface and the EPMA compositional mapping of different elements, as well as the line scanning through the brighter region of $Sn_{0.85}Sb_{0.15}Te$ sample. The composition of the brighter regions in BSE image is different from the matrix. A line scanning is conducted from Point 1 to Point 2 in the inset of Fig. 1d, and a higher content of Sb plateau appears in the brighter region ($\sim$8 μm). According to the EPMA results, the composition of the brighter region ought to be $Sn_{0.11}Sb_{0.60}Te_{0.29}$. It could be explained as Sb_2Te with a small amount of dissolving Sn based on the SnTe-Sb_2Te_3 pseudo-binary phase diagram (Fig. 1e) [49], where the cooling process takes place along the arrow (Sn $\sim$ 42.5 at%). When the temperature cools down to near 1,000 K, the SnTe phase increases steadily, and a peritectic reaction emerges at about 879 K, which results in the formation of Sb_2Te/SbTe. At 873 K, a eutectic reaction happens and a little amount of Sb_2Te_3 separates out and Sb_2Te/SbTe phases continue to increase. In the meanwhile, Sn diffuses in all kinds of phases with time and the brighter region with high Sb content forms eventually. All the EPMA compositions (both the matrix and the white region) are listed in Table S1 (online). Based on the above discussion, the impurity peaks in XRD may result from both the micro- and nano-precipitates.

As shown in Fig. 1f, the lattice parameter follows the Vegard's law and decreases with the addition of Mg because that the ionic radius of Mg (0.086 nm) is smaller than that of Sn (0.093 nm) [34]. It is in accordance with the XRD result in which the peaks shift to higher angles with the increase of Mg content (Fig. S1 online), indicating that Mg is indeed alloyed in SnTe and the solubility limit of Mg in SnTe is no less than 10 at%, consistent with the

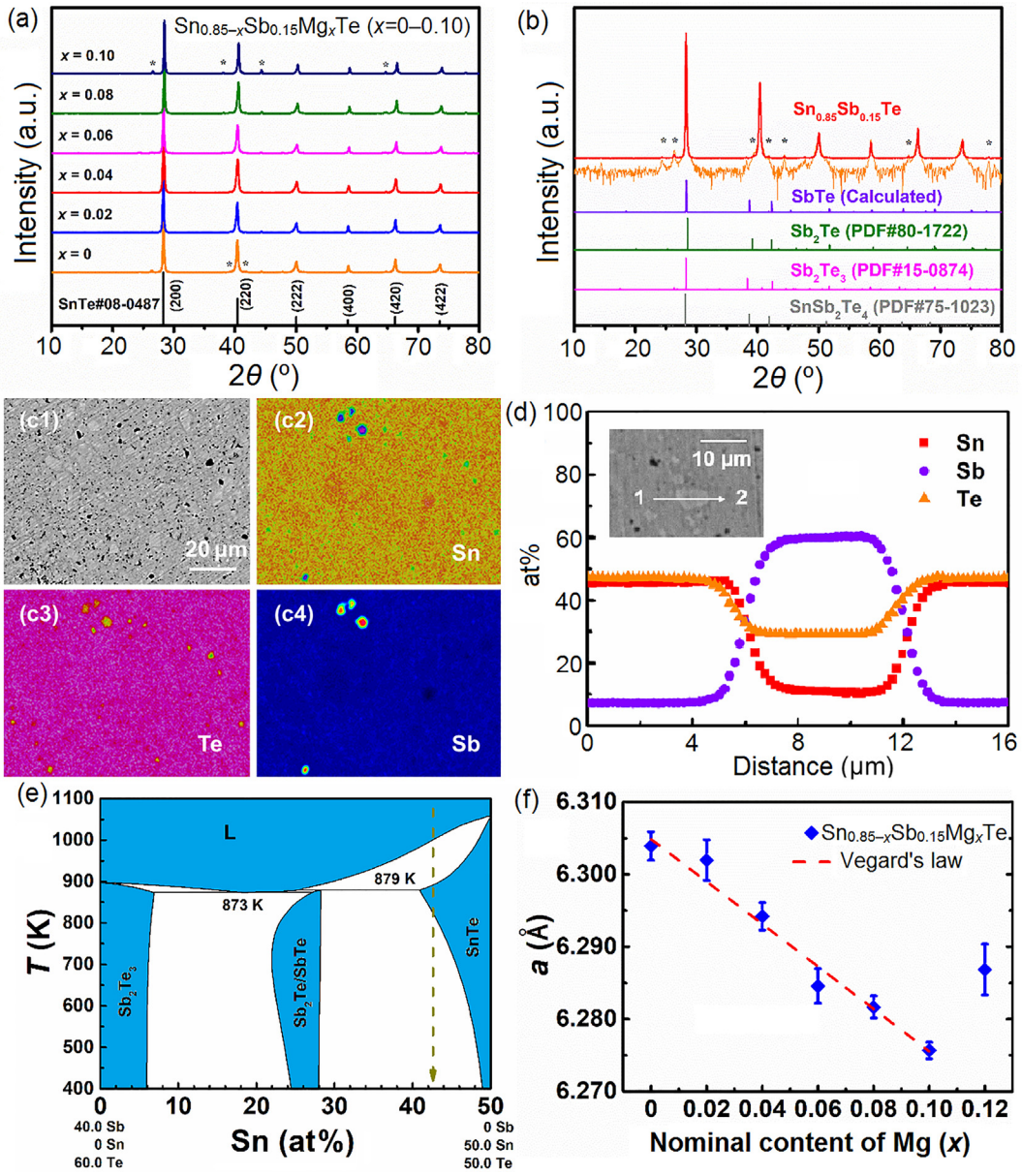

Fig. 1. (Color online) (a) XRD patterns of $Sn_{0.85-x}Sb_{0.15}Mg_xTe$ (x = 0–0.10). A trace of second phases can be found in all samples and at x = 0.10, the peaks of second phases rises obviously. (b) The comparison between the logarithm curve of $Sn_{0.85}Sb_{0.15}Te$ and some possible phases' standard patterns. The second phases cannot be identified exactly but they may be the mixture of several phases. (c1) The back-scattering electron image of the polished surface and (c2–c4) the EPMA different elements compositional mapping of $Sn_{0.85}Sb_{0.15}Te$. (d) The line scanning of the brighter region from Point 1 to 2 in the inset BSE image. (e) Pseudo-binary phase diagram of Sb_2Te_3-SnTe [49]. (f) The lattice parameters of $Sn_{0.85-x}Sb_{0.15}Mg_xTe$ (x = 0–0.12).

results observed by Banik et al. [34]. But at x = 0.10, a larger amount of second phase was observed as seen in Fig. 1a. This is probably because of the competitive relationship between Mg and Sb co-substituting the Sn sites, and the excessive Mg lowers the solubility of Sb in SnTe, resulting in more second phases.

3.2. Thermal conductivity

The temperature dependences of total thermal conductivity and lattice thermal conductivity for the $Sn_{0.85-x}Sb_{0.15}Mg_xTe$ specimens are shown in Fig. 2. The lattice thermal conductivity κ_L is derived by subtracting the electronic thermal conductivity κ_e from the total thermal conductivity κ. κ_e is calculated by the Wiedemann-Franz relationship, $\kappa_e = L\sigma T$, where L is the Lorenz number. L can be derived with the single parabolic band (SPB) model assuming that acoustic phonon scattering dominates the charge transport [50].

The thermal conductivity of all samples decreases with increasing temperature as shown in Fig. 2a. The alloying of Mg reduces κ nearly 45% from ~3.03 to ~1.68 W m^{-1} K^{-1} at room temperature, which is ascribed to both the reduction of κ_e and κ_L (Fig. 2b and c). The reduction of κ_e is mainly caused by the reduction of σ, which will be discussed later.

As shown in Fig. 2c, pure polycrystalline SnTe has a high κ_L, which exhibits a temperature dependence of $\kappa_L \propto T^{-1}$, indicating that phonon–phonon Umklapp scattering is the dominant phonon scattering mechanism. The Sb alloying not only reduces κ_L substantially, but also makes the temperature dependence of κ_L flatter due to the enhanced point defect scattering of Sb_{Sn} and the second phase scattering of endotaxial Sb rich nano-precipitates [36] and micro-

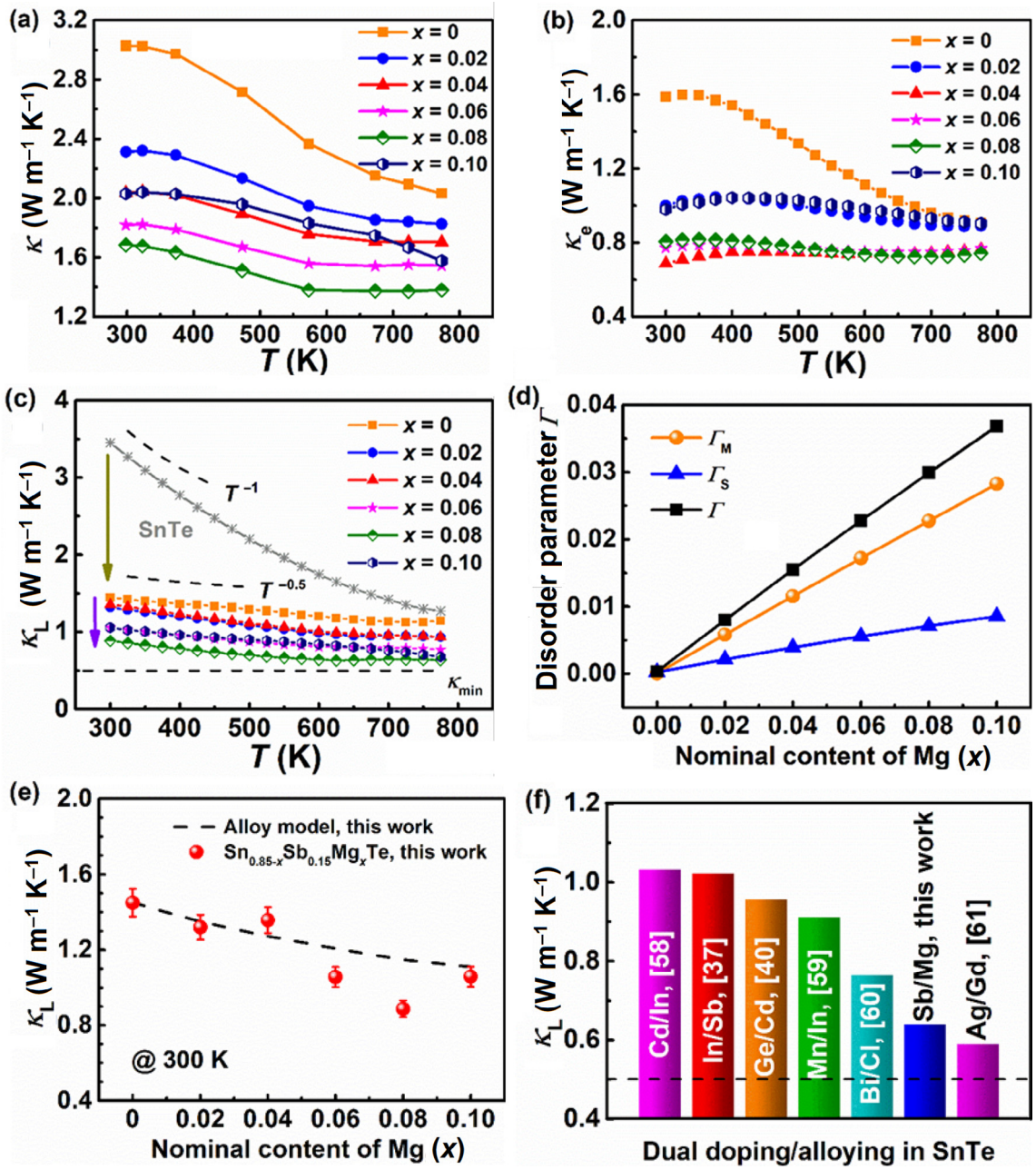

Fig. 2. (Color online) Temperature dependences of (a) the total thermal conductivity, (b) the electronic thermal conductivity and (c) the lattice thermal conductivity. In Fig. 2c, the grey line is the lattice thermal conductivity of pristine SnTe sample by contrast and the κ_{min} is the minimum theoretical lattice thermal conductivity calculated by Cahill model [57]. (d) The Mg content dependences of the disorder scattering parameter Γ, the mass fluctuations scattering parameter Γ_M and the strain field fluctuations scattering parameter Γ_S. (e) The composition-dependent κ_L at 300 K and the model prediction calculated by alloy model. (f) The comparison of the minimum κ_L of different dual-doping/alloying in SnTe-based systems, including Cd/In [58], In/Sb [37], Ge/Cd [40], Mn/In [59], Bi/Cl [60] and Ag/Gd [61].

domains. Furthermore, κ_L continues to decrease with increasing Mg content, revealing that the point defect scattering caused by the Mg_{Sn} has also non-negligible influence on phonon transport.

In order to confirm that the contribution of Mg alloying to the point-defect scattering in $Sn_{0.85}Sb_{0.15}Te$, the disorder scattering parameter Γ is calculated as $\Gamma = \Gamma_M + \Gamma_S$, where Γ_M and Γ_S are mass fluctuation scattering parameter and strain field fluctuation scattering parameter, respectively [51–55]. The calculation process is presented in Supplementary Information (online) and the related calculated data are listed in Table S2 (online).

For $Sn_{0.85-x}Sb_{0.15}Mg_xTe$, there are two sublattices (Sn site and Te site) and three atoms (Sn, Sb and Mg) occupy Sn site. The disorder parameter Γ versus the content of Mg is shown in Fig. 2d, in which all three disorder parameters Γ_M, Γ_S and Γ increase remarkably with Mg alloying. Sn and Sb are two neighbor elements in the periodic table of elements, and their atom masses and ionic radii are nearly the same (Sn: 116.71 g mol^{-1}, ~0.093 nm [34]; Sb: 121.76 g mol^{-1}, ~0.092 nm [56]), resulting in a small mass and strain field fluctuations in SnTe matrix. However, Mg possesses a lighter mass and a smaller radius (24.305 g mol^{-1}, ~0.086 nm [34]). With increasing Mg content, the degree of disorder increases and the mass fluctuation takes the leading position. The disorder parameter multiplies from 0.0004 of $Sn_{0.85}Sb_{0.15}Te$ to 0.0368 of $Sn_{0.75}Sb_{0.15}Mg_{0.10}Te$ with a nearly hundredfold rise, contributing to the great enhancement of point-defect scattering and the decrease of the lattice thermal conductivity.

Taking $Sn_{0.85}Sb_{0.15}Te$ as the matrix and Mg as the alloy element to study the contribution of point defect scattering induced by Mg, the alloy model is also calculated to predict the theoretical lattice thermal conductivity of $Sn_{0.85-x}Sb_{0.15}Mg_xTe$ at 300 K, based on Debye-Callaway model in Fig. 2e (details are given in Supplementary Information, online). The calculation result is basically consistent with the experimental data (the deviation is probably caused by the little amount variation of the second phases), demonstrating that Mg_{Sn} defect is a significant factor on the reduction of $Sn_{0.85-x}Sb_{0.15}Mg_xTe$. Typically, at $x = 0.08$, κ_L at room temperature reaches $\sim 0.89\ W\ m^{-1}\ K^{-1}$ and decreases to $\sim 0.64\ W\ m^{-1}\ K^{-1}$ at 773 K, which is near the theoretical minimum of the lattice thermal conductivity κ_{min} ($\sim 0.5\ W\ m^{-1}\ K^{-1}$) of SnTe calculated by using the Cahill model [57]. Fig. 2f shows the comparison of the minimum lattice thermal conductivities of some typical dual alloying or doping in SnTe-based system, indicating that the Sb and Mg co-alloying SnTe in this work has a quite low κ_L [37,40,58–61].

3.3. Electrical properties

Fig. 3 illustrates the electrical properties of all $Sn_{0.85-x}Sb_{0.15}Mg_xTe$ ($x = 0$–0.10) samples. Compared with the pristine SnTe ($\sim 79.7 \times 10^4\ S\ m^{-1}$), the room temperature electrical conductivity of $Sn_{0.85}Sb_{0.15}Te$ ($\sim 23.5 \times 10^4\ S\ m^{-1}$) has already fallen steeply due to the decreased carrier concentration by aliovalent doping of Sb at Sn site (Fig. 3a). With the increase of Mg content, the electrical conductivity diminishes first and ascents slightly at $0.04 \le x \le 0.08$. The carrier concentration n_H and the carrier mobility μ_H are plotted in Fig. 3b. Except for abnormal abrupt augment of the last sample due to the increase of the second phase, the carrier concentration varies slightly between 2.45 and $1.86 \times 10^{20}\ cm^{-3}$ (around the optimal carrier concentration for SnTe).

Mg is isovalent to Sn and Mg alloying would not lead to an enormous change in n_H. However, once adding Mg in $Sn_{0.85}Sb_{0.15}Te$, the carrier mobility μ_H decreases obviously and the Seebeck coefficient increases (Fig. 3c), indicating that the density-of-state (DOS) effective mass m^* increases with Mg alloying. The quantitative calculation of the DOS effective mass in SnTe requires the consideration of the influence of two valence bands, but for simplicity the SPB model is used here [34]. As listed in Table 1, the addition of Mg increases m^* from $0.9m_e$ to $1.2m_e$, which can be ascribed to the band convergence of heavy valence band Σ and light valence band L in SnTe [34]. However, the increase in DOS effective mass is not systematic with Mg content, possibly due to the non-systematic deviation from the nominal compositions.

Table 1
The carrier concentration and the DOS effective mass m^*

Nominal composition	n_H ($\times 10^{20}\ cm^{-3}$)	m^* (m_e)
$Sn_{0.85}Sb_{0.15}Te$	2.45	0.90
$Sn_{0.83}Sb_{0.15}Mg_{0.02}Te$	2.27	1.17
$Sn_{0.81}Sb_{0.15}Mg_{0.04}Te$	1.93	1.22
$Sn_{0.79}Sb_{0.15}Mg_{0.06}Te$	1.86	1.15
$Sn_{0.77}Sb_{0.15}Mg_{0.08}Te$	1.95	1.12
$Sn_{0.85}Sb_{0.15}Te$ [36]	2.34	0.61
$Sn_{0.85}Sb_{0.15}Te$ [37]	3.85	0.99

Fig. 3d shows the Pisarenko curve and some representative works of alloying or doping in SnTe at room temperature [34,36,44,58,62–64]. The undoped SnTe is synthesized by different methods to yield a various range of carrier concentration [62,63], which conforms to the theoretical curve. So are some doping samples like Bi-doped SnTe [64]. However, other data lie above the curve for different reasons, for example, valence band convergence of Mg alloying and resonant level of In doping [34,44]. Dual doping leads to a higher Seebeck coefficient at the same carrier concentration, like Cd-In co-doping [58] and the case in this work (Sb and Mg alloying). A maximum of Seebeck coefficient is 184 μV K^{-1} at 773 K of $Sn_{0.79}Sb_{0.15}Mg_{0.06}Te$.

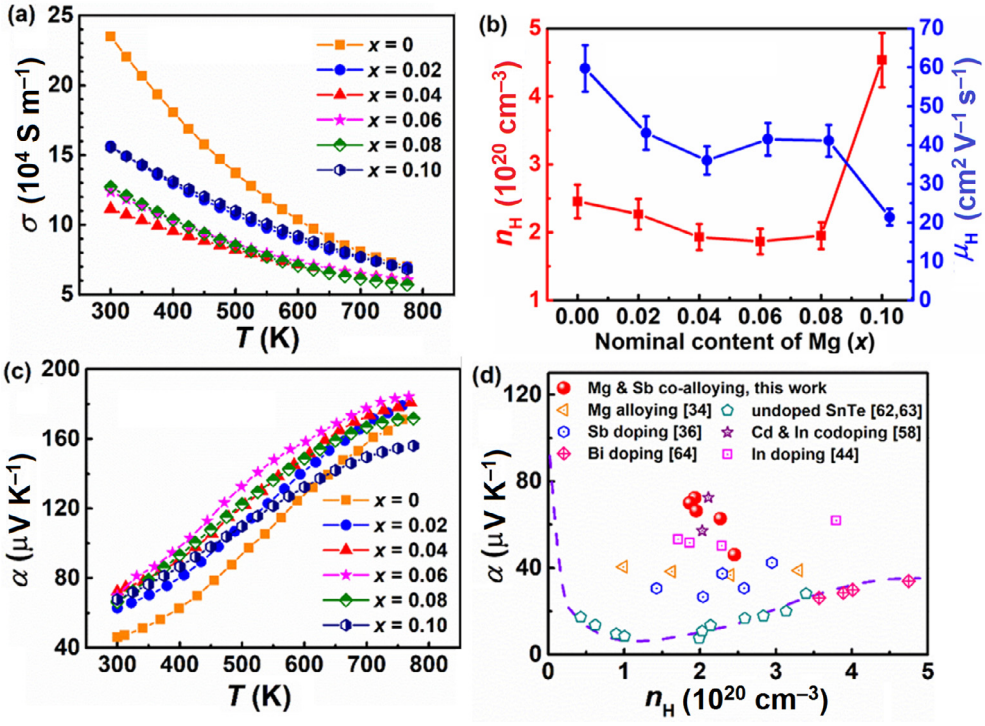

Fig. 3. (Color online) Temperature dependences of the electrical conductivity (a), and the Seebeck coefficient of $Sn_{0.85-x}Sb_{0.15}Mg_xTe$ (c). (b) The variation of the carrier concentration and mobility with Mg content. (d) The Pisarenko curve (dash line) calculated by Zhang et al. [44] and some representative work of alloying or doping in SnTe at room temperature [34,36,58,62–64].

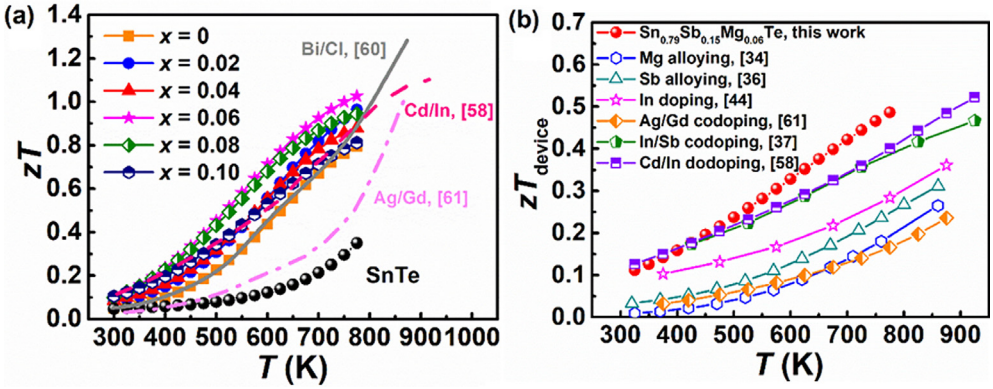

Fig. 4. (Color online) (a) Temperature dependences of the figure of merit zT of $Sn_{0.85-x}Sb_{0.15}Mg_xTe$ [58,60,61]. (b) The device zT_{device} of different SnTe-based compositions, including Mg alloying [34], Sb alloying [36], In doping [44], Ag/Gd codoping [61], In/Sb codoping [37], and Cd/In codoping [58] for comparison.

3.4. The figure of merit zT

The figure of merit zT versus temperature of $Sn_{0.85-x}Sb_{0.15}Mg_xTe$ is shown in Fig. 4a. Sb alloying optimizes the carrier concentration of SnTe and diminishes the lattice thermal conductivity. And Mg alloying further reduces κ_L by point-defect scattering due to mass and strain field fluctuations and raises the Seebeck coefficient by band convergence, which make the maximum zT_{max} increase from 0.35 for SnTe to 0.79 for $Sn_{0.85}Sb_{0.15}Te$, and then to 1.02 for $Sn_{0.79}Sb_{0.15}Mg_{0.06}Te$ at 773 K. And some typical works on dual doping in SnTe are also present for comparison [58,60,61]. As is seen, although the zT_{max} values of other works are almost the same or even higher than this work at higher temperatures (873 or 923 K), the zT value of $Sn_{0.79}Sb_{0.15}Mg_{0.06}Te$ is higher than other works at the whole temperature range 300–773 K yet, indicating the superiority of this composition at relative low temperatures. In addition, the deformation, microcracks and softening will occur in the SnTe samples above about 873 K, as shown in Fig. S3 (online), resulting in the unreliable measurements. So we usually set the maximum measurement temperature not higher than 823 K, usually 773 K as this work.

To compare with other SnTe-based materials in application potential, the device zT_{device} is calculated by the method presenting in Ref. [65]. As is seen in Fig. 4b, the maximum device zT_{device} reaches ~0.50 and lies above others typical SnTe-based systems consistently, revealing that this SnTe-based composition has a promising application in intermediate temperature [34,36,37,44,58,61].

4. Conclusions

A series of p-type $Sn_{0.85-x}Sb_{0.15}Mg_xTe$ (x = 0–0.10) TE materials were synthesized and studied for the first time. Sb alloying optimizes the hole carrier concentration of SnTe, and decreases the lattice thermal conductivity simultaneously. Moreover, because of the large mass and radius differences between Mg and Sn, the Mg alloying induces a nearly hundredfold rise in disorder parameter and further lower the lattice thermal conductivity down to approximately 0.64 $W\,m^{-1}\,K^{-1}$ at 773 K. Additionally, Mg alloying synergistically enhances the Seebeck coefficient resulting from the band convergence. The maximum zT_{max} of 1.02 at 773 K and the device zT_{device} of ~0.50 for $Sn_{0.79}Sb_{0.15}Mg_{0.06}Te$ are obtained, which indicates this SnTe-based composition has an application potential in intermediate temperature TE power generation.

Conflict of interest

The authors declare that they have no conflict of interest.

Acknowledgments

This work was supported by the National Key Research and Development Program of China (2018YFB0703600), the National Science Fund for Distinguished Young Scholars (51725102), and the National Natural Science Foundation of China (51861145305, 51761135127, and 51871199).

Author contributions

Tiezheng Fu designed and fabricated the samples. Teng Fang helped to test some properties of the samples. Jiazhan Xin and Jiajun Shen put forward much deeper analysis of the results. Tiezheng Fu wrote the paper with the direction and support from Tiejun Zhu and Xinbing Zhao. All authors contributed to the general discussion.

Appendix A. Supplementary data

Supplementary data to this article can be found online at https://doi.org/10.1016/j.scib.2019.06.007.

References

[1] Shi X, Chen L, Uher C. Recent advances in high-performance bulk thermoelectric materials. Int Mater Rev 2016;61:379–415.
[2] Zhu T, Liu Y, Fu C, et al. Compromise and synergy in high-efficiency thermoelectric materials. Adv Mater 2017;29:1605884.
[3] Xin J, Tang Y, Liu Y, et al. Valleytronics in thermoelectric materials. NPJ Quantum Mater 2018;3:9.
[4] Zhang Q, Bai S, Chen L. Technologies and applications of thermoelectric devices: Current status, challenges and prospects. J Inorg Mater 2019;34:279–93.
[5] Xiong J, Han C, Li Z, et al. Effects of nanostructure on clean energy: big solutions gained from small features. Sci Bull 2015;60:2083–90.
[6] Bell L. Cooling, heating, generating power, and recovering waste heat with thermoelectric systems. Science 2008;321:1457–61.
[7] Petsagkourakis I, Tybrandt K, Crispin X, et al. Thermoelectric materials and applications for energy harvesting power generation. Sci Technol Adv Mater 2018;19:836–62.
[8] Mori T, Priya S. Materials for energy harvesting: at the forefront of a new wave. MRS Bull 2018;43:176–80.
[9] Shen J, Fang T, Fu T, et al. Lattice thermal conductivity in thermoelectric materials. J Inorg Mater 2019;34:260–8.
[10] Fang T, Zhao X, Zhu T. Band structures and transport properties of high-performance half-Heusler thermoelectric materials by first principles. Materials 2018;11:847.
[11] Fu C, Wu H, Liu Y, et al. Enhancing the figure of merit of heavy-band thermoelectric materials through hierarchical phonon scattering. Adv Sci 2016;3:1600035.
[12] Zhao L, Chang C, Tan G, et al. SnSe: a remarkable new thermoelectric material. Energy Environ Sci 2016;9:3044–60.
[13] Zhai R, Wu Y, Zhu T, et al. Thermoelectric performance of p-type zone-melted Se-doped $Bi_{0.5}Sb_{1.5}Te_3$ alloys. Rare Met 2018;37:308–15.
[14] Nshimyimana E, Su X, Xie H, et al. Realization of non-equilibrium process for high thermoelectric performance Sb-doped GeTe. Sci Bull 2018;63:717–25.
[15] Guan M, Qiu P, Song Q, et al. Improved electrical transport properties and optimized thermoelectric figure of merit in lithium-doped copper sulfides. Rare Met 2018;37:282–9.

[16] Zhu T, Hu L, Zhao X, et al. New insights into intrinsic point defects in V_2VI_3 thermoelectric materials. Adv Sci 2016;3:1600004.
[17] Xu P, Fu T, Xin J, et al. Anisotropic thermoelectric properties of layered compound $SnSe_2$. Sci Bull 2017;62:1663–8.
[18] Tang H, Dong J, Sun F, et al. Adjusting Na doping *via* wet-chemical synthesis to enhance thermoelectric properties of polycrystalline SnS. Sci China Mater 2019. https://doi.org/10.1007/s40843-018-9392-7.
[19] Liu Y, Fu C, Xia K, et al. Lanthanide contraction as a design factor for high-performance half-Heusler thermoelectric materials. Adv Mater 2018;30:1800881.
[20] Wang H, Luo X, Chen W, et al. Magnetic-field enhanced high-thermoelectric performance in topological dirac semimetal Cd_3As_2 crystal. Sci Bull 2018;63:411–8.
[21] Mao J, Liu Z, Zhou J, et al. Advances in thermoelectrics. Adv Phys 2018;67:69–147.
[22] Mori T. Novel principles and nanostructuring methods for enhanced thermoelectrics. Small 2017;13:1702013.
[23] Tan G, Shi F, Hao S, et al. Non-equilibrium processing leads to record high thermoelectric figure of merit in PbTe-SrTe. Nat Commun 2016;7:12167.
[24] Chen Z, Jian Z, Li W, et al. Lattice dislocations enhancing thermoelectric PbTe in addition to band convergence. Adv Mater 2017;29:1606768.
[25] Fu L, Yin M, Wu D, et al. Large enhancement of thermoelectric properties in *n*-type PbTe via dual-site point defects. Energy Environ Sci 2017;10:2030–40.
[26] Zhang J, Wu D, He D, et al. Extraordinary thermoelectric performance realized in *n*-type PbTe through multiphase nanostructure engineering. Adv Mater 2017;29:1703148.
[27] Fu T, Yue X, Wu H, et al. Enhanced thermoelectric performance of PbTe bulk materials with figure of merit zT>2 by multi-functional alloying. J Materiomics 2016;2:141–9.
[28] Moshwan R, Yang L, Zou J, et al. Eco-friendly SnTe thermoelectric materials: progress and future challenges. Adv Funct Mater 2017;27:1703278.
[29] Li S, Li X, Ren Z, et al. Recent progress towards high performance of tin chalcogenide thermoelectric materials. J Mater Chem A 2018;6:2432–48.
[30] Brebrick RF. Deviations from stoichiometry and electrical properties in SnTe. J Phys Chem Solids 1963;24:27–36.
[31] Zhou M, Gibbs ZM, Wang H, et al. Optimization of thermoelectric efficiency in SnTe: the case for the light band. Phys Chem Chem Phys 2014;16:20741–8.
[32] Hu H, Yang J, Xin J, et al. High thermoelectric performance of SnTe from the disproportionation of SnO. J Inorg Mater 2019;34:315–20.
[33] Al Orabi RAR, Mecholsky NA, Hwang J, et al. Band degeneracy, low thermal conductivity, and high thermoelectric figure of merit in SnTe-CaTe alloys. Chem Mater 2016;28:376–84.
[34] Banik A, Shenoy US, Anand S, et al. Mg alloying in SnTe facilitates valence band convergence and optimizes thermoelectric properties. Chem Mater 2015;27:581–7.
[35] Li W, Chen Z, Lin S, et al. Band and scattering tuning for high performance thermoelectric $Sn_{1-x}Mn_xTe$ alloys. J Materiomics 2015;1:307–15.
[36] Banik A, Vishal B, Perumal S, et al. The origin of low thermal conductivity in $Sn_{1-x}Sb_xTe$: phonon scattering via layered intergrowth nanostructures. Energy Environ Sci 2016;9:2011–9.
[37] Wang D, Zhang X, Yu Y, et al. Enhancing thermoelectric performance of SnTe via stepwisely optimizing electrical and thermal transport properties. J Alloy Compd 2019;773:571–84.
[38] Pei Y, Zheng L, Li W, et al. Interstitial point defect scattering contributing to high thermoelectric performance in SnTe. Adv Electron Mater 2016;2:1600019.
[39] Tan G, Zhao L, Shi F, et al. High thermoelectric performance of *p*-type SnTe via a synergistic band engineering and nanostructuring approach. J Am Chem Soc 2014;136:7006–17.
[40] Tang J, Gao B, Lin S, et al. Manipulation of solubility and interstitial defects for improving thermoelectric SnTe alloys. ACS Energy Lett 2018;3:1969–74.
[41] Wu H, Chang C, Feng D, et al. Synergistically optimized electrical and thermal transport properties of SnTe via alloying high-solubility MnTe. Energy Environ Sci 2015;8:3298–312.
[42] Tan G, Shi F, Hao S, et al. Valence band modification and high thermoelectric performance in SnTe heavily alloyed with MnTe. J Am Chem Soc 2015;137:11507–16.
[43] Guo F, Cui B, Liu Y, et al. Thermoelectric SnTe with band convergence, dense dislocations, and interstitials through Sn self-compensation and Mn alloying. Small 2018;14:1802615.
[44] Zhang Q, Liao B, Lan Y, et al. High thermoelectric performance by resonant dopant indium in nanostructured SnTe. Proc Natl Acad Sci USA 2013;110:13261–6.
[45] Pei Y, LaLonde A, Iwanaga S, et al. High thermoelectric figure of merit in heavy hole dominated PbTe. Energy Environ Sci 2011;4:2085–9.
[46] Pei Y, LaLonde AD, Wang H, et al. Low effective mass leading to high thermoelectric performance. Energy Environ Sci 2012;5:7963–9.
[47] Blachnik R, Igel R. Thermodynamic properties of IV-VI compounds: lead chalcogenides. Zeitschrift Fur Naturforschung B-J Chem Sci 1974;29:625–9.
[48] Yang S, Zhu T, Sun T, et al. Nanostructures in high-performance $(GeTe)_x(AgSbTe_2)_{100-x}$ thermoelectric materials. Nanotechnology 2008;19:245707.
[49] Stegherr A. Das dreistoffsystem zinn-antimon-tellur. Philips Res Rep 1969;6:1–71.
[50] Xia K, Liu Y, Anand S, et al. Enhanced thermoelectric performance in 18-electron $Nb_{0.8}CoSb$ half-Heusler compound with intrinsic Nb vacancies. Adv Funct Mater 2018;28:1705845.
[51] Cahill DG, Watson SK, Pohl RO. Lower limit to the thermal conductivity of disordered crystals. Phys Rev B 1992;46:6131–40.
[52] Tan G, Shi F, Hao S, et al. Codoping in SnTe: enhancement of thermoelectric performance through synergy of resonance levels and band convergence. J Am Chem Soc 2015;137:5100–12.
[53] Wang L, Tan X, Liu G, et al. Manipulating band convergence and resonant state in thermoelectric material SnTe by Mn–In codoping. ACS Energy Lett 2017;2:1203–7.
[54] Zhou Z, Yang J, Jiang Q, et al. Enhanced thermoelectric performance of SnTe: high efficient cation-anion co-doping, hierarchical microstructure and electro-acoustic decoupling. Nano Energy 2018;47:81–8.
[55] Zhang L, Wang J, Cheng Z, et al. Lead-free SnTe-based thermoelectrics: enhancement of thermoelectric performance by doping with Gd/Ag. J Mater Chem A 2016;4:7936–42.
[56] Slack GA. Effect of isotopes on low-temperature thermal conductivity. Phys Rev 1957;105:829–31.
[57] Abeles B. Lattice thermal conductivity of disordered semiconductor alloys at high temperatures. Phys Rev 1963;131:1906–11.
[58] Wang H, LaLonde AD, Pei Y, et al. The criteria for beneficial disorder in thermoelectric solid solutions. Adv Funct Mater 2013;23:1586–96.
[59] Yang J, Meisner GP, Chen L. Strain field fluctuation effects on lattice thermal conductivity of ZrNiSn-based thermoelectric compounds. Appl Phys Lett 2004;85:1140.
[60] Shen J, Fu C, Liu Y, et al. Enhancing thermoelectric performance of FeNbSb half-Heusler compound by Hf-Ti dual-doping. Energy Storage Mater 2018;10:69–74.
[61] Zhu B, Xie C, Zeng D, et al. Investigation of gas sensitivity of Sb-doped ZnO nanoparticles. Mater Chem Phys 2005;89:148–53.
[62] Brebrick RF, Strauss AJ. Anomalous thermoelectric power as evidence for two-valence bands in SnTe. Phys Rev 1963;131:104–10.
[63] Kafalas JA, Brebrick RF, Strauss AJ. Evidence that SnTe is a semiconductor. Appl Phys Lett 1964;4:93–4.
[64] Galushchak M, Freik D, Ivanyshyn I, et al. Thermoelectric properties and defective subsystem in doped telluride of tin. J Thermoelec 2000:42–50.
[65] Snyder GJ, Snyder AH. Figure of merit zT of a thermoelectric device defined from materials properties. Energy Environ Sci 2017;10:2280–3.

Tiezheng Fu is a Ph.D. candidate in Materials Science at Zhejiang University. His research focuses on IV-VI thermoelectric compounds under the supervision of Prof. Xinbing Zhao and Prof. Tiejun Zhu. He was awarded Bachelor of Engineering Degree in Materials Science and Engineering from Zhejiang University in 2014.

Tiejun Zhu is a Professor of Materials Science and Engineering at Zhejiang University. He obtained his Ph. D. degree from Zhejiang University in 2001. He was a research fellow in Singapore-MIT Alliance from 2002 to 2004, and a visiting scientist in California Institute of Technology in 2011. He has been a faculty member in Zhejiang University since 2004. His current research is on the advanced fabrication, microstructure and transport mechanisms of high efficiency thermoelectric materials.

Xinbing Zhao is the Qiushi Distinguished Professor of Materials Science and Engineering at Zhejiang University. He earned his Ph.D. degree in Materials Science and Engineering in 1990 from Zhejiang University and was a doctoral student in the Institute of Metallurgy and Metal Physics in RWTH Aachen, Germany from 1987 to 1990. His research focuses on materials synthesis, characterization, and applications, with a particular focus on energy materials including thermoelectrics and lithium ion batteries.